Journal of Thermal Science Vol.24, No.3 (2015) 239–245

DOI: 10.1007/s11630-015-0779-x **Article ID: 1003-2169(2015)03-0239-07**

Unsteady Flow Analysis of an Axial Flow Hydraulic Turbine with Collection Devices Comprising a Different Number of Blades

Yasuyuki Nishi[1], Terumi Inagaki[1], Yanrong Li[1], Sou Hirama[2] and Norio Kikuchi[3]

1. Department of Mechanical Engineering, Ibaraki University, 4-12-1 Nakanarusawa-cho, Hitachi-shi, Ibaraki, 316-8511, JAPAN

2. Graduate School of Science and Engineering, Ibaraki University, 4-12-1 Nakanarusawa-cho, Hitachi-shi, Ibaraki, 316-8511, JAPAN

3. Ibasei, Ltd., 4-7-10 Kamine-cho, Hitachi-shi, Ibaraki, 317-0064, JAPAN

We previously devised a new type of portable hydraulic turbine that uses the kinetic energy of an open-channel flow to improve output power by catching and accelerating the flow. The turbine contains an axial flow runner with an appended collection device and a diffuser section that is not axisymmetric. The objective of this study is to determine how interference between the collection device and the runner influences performance characteristics of the turbine. We investigated the performance characteristics of the turbine and flow field for different numbers of blades during both unsteady and steady flow. During an unsteady flow, the maximum values of power coefficients for three and two blades increased by approximately 8.8% and 21.4%, respectively, compared to those during a steady flow. For the three-blade runner, the power coefficient showed small fluctuations, but for the two-blade runner, the power coefficient showed large fluctuations. These fluctuations in the power coefficient are attributed to fluctuations in the loading coefficient, which were generated by interference between the runner and the diffuser section of the collection device.

Keywords: Hydraulic Turbine, Runner, Collection Device, Performance, Unsteady Flow Analysis

Introduction

Hydraulic turbines used for hydropower generation are broadly classified into those for pipe conduits[1] and those for open channels[2-4]. Turbines for pipe conduits store water in dams and water tanks, and move the water using the stored potential energy. Hence, the number of construction sites with sufficient head of water and little impact on the ecosystem is small. On the other hand, turbines for open channels do not require ancillary facilities for water transmission, and it is possible to generate power with a small head of water. However, turbine rotation speeds are low and the turbines themselves tend to be large, so available installation sites are limited. Recently, despite the development of turbines that can generate power simply by being placed in the path of flow[5-7], the available turbine output power per unit water-receiving area is inadequate.

We have proposed a new type of hydraulic turbine that uses the kinetic energy of flow in open channels by applying the principle of a wind turbine with diffuser[8] with an attached brim[9]. To improve output power, the turbine contains an axial flow runner with an appended collection device that includes a diffuser section to accelerate the flow. Performance and flow fields for the runner, collection device, and their composite body have been stu-

Received: October 2014 Yasuyuki Nishi: Associate Professor

Nomenclature

A	water-receiving area (m^2) $=\pi r_t^2$	λ	tip speed ratio = $r_t\omega/v_\infty$
C_I	input power coefficient $=\left(\overline{P_1}-\overline{P_2}\right)Q\Big/\left(\rho A v_\infty^3/2\right)$	ν	hub ratio = r_h/r_t
C_P	pressure coefficient $=\left(P-P_\infty\right)\Big/\left(\rho v_\infty^2/2\right)$	ρ	fluid density (kg/m^3)
C_W	power coefficient $=W\Big/\left(\rho A v_\infty^3/2\right)$	ψ	loading coefficient $=\left(\overline{P_1}-\overline{P_2}\right)\Big/\left(\rho \overline{v_{a1}}^2/2\right)$
K	inlet velocity ratio $=\overline{v_{a1}}/v_\infty$	ω	rotational angular velocity (rad/s)
n	rotational speed (min^{-1})	**Subscripts**	
P	static pressure (gauge pressure) (Pa)	1	just before the runner
Q	flow rate through the runner (m^3/s) $=A\overline{v_{a1}}$	2	just after the runner
r	runner radius (m)	3	collection device outlet
v	absolute velocity (m/s)	a	axial component
W	output power (W)	h	hub
Greek letters		t	tip
η	turbine efficiency $=C_W/C_I$	∞	infinite distance
θ^*	blade phase angle (°)	$\overline{\ }$	average value for the flow rate

died during a steady flow[9-10]. The effectiveness of the design was verified[9-10], and the influence of the number of blades was determined[11]. However, in the collection device, the diffuser section is not axisymmetric; therefore, an unsteady flow is generated by interference between the runner and the collection device. This unsteady flow must be taken into account for more detailed performance evaluations.

The objective of this study is to determine the influence of interference between the collection device and the runner; the latter influences the performance characteristics of an axial flow hydraulic turbine. We investigated the performance characteristics of the turbine and the flow field for runners with different numbers of blades during an unsteady flow and compared the results with those obtained during a steady flow.

Hydraulic Turbine Test Piece

A schematic of the hydraulic turbine test piece is shown in Fig. 1, and the coordinate system adopted for the analysis is shown in Fig. 2. The turbine uses the principles of the wind turbine with diffuser [8] with an attached brim and comprises a collection device (C.D.) appended to an axial flow runner. The hydraulic turbine was designed for a flow speed v_∞ of 1.5 m/s and open-channel installation in a water depth of 400 mm. The blade phase angle θ^* was taken to be positive from the z-axis counterclockwise when viewed from the inlet side. When the reference blade is positioned in the positive direction of the z-axis (the position in Fig. 5 described below), θ^* is defined to be 0°.

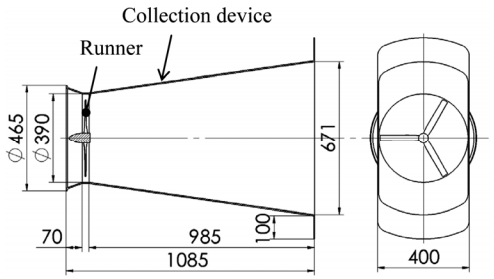

Fig. 1 Hydraulic turbine

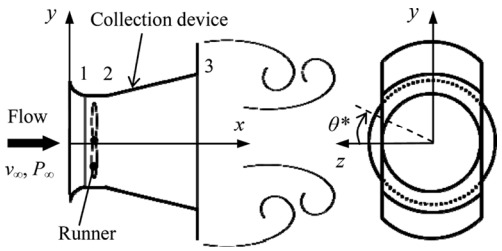

Fig. 2 The definition of a coordinate system

An overview of the collection device is shown in Fig. 3. The collection device was composed of an inlet nozzle, a diffuser, and a brim. The total length was 1085 mm. Open and shallow water channels are constrained in the height direction. Accordingly, the type described here differs from conventional wind turbines[8, 12-14] and hydraulic turbines[15-18] in which the diffuser section of the collection device is constant vertically and varies horizontally. Thus, it is possible to make the runner outer diameter almost as large as the water depth by making the height of the diffuser section the same as the water depth. The height of the diffuser section was 400 mm to

match the design water depth and the spread angle was 8.1°. The brim section consisted of two brims mounted on the left and right sides of the outlet of the collection device. The length of each brim was 100 mm.

Two types of runners were used in this study and are illustrated in Figs. 4(a) and 4(b). Runner A contained three blades that were designed based on the blade element momentum theory[9-10]. To maximize the output power, the outer diameter of the runner was designed to approximately match the designed water depth. Emphasizing the importance of strength when water flow is considered, MEL021[19] was adopted for the airfoil of the blade, which has a maximum blade thickness relative to the chord length. The design angle of attack is 5°. Runner B was a two-blade runner that was simply designed based on the three blades of runner A.

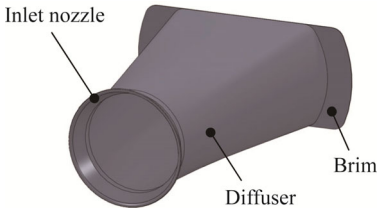

Fig. 3 Collection device

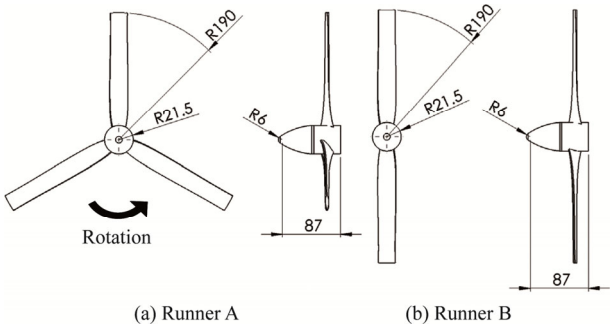

Fig. 4 Runners

Numerical Analysis

The general-purpose thermal fluid analysis code ANSYS CFX15.0 was used in the numerical analyses. Three-dimensional steady and unsteady flow analyses were performed for the composite body of the hydraulic turbine. The basic equations are the conservation of mass equation and the conservation of momentum equation, and the SST (Shear Stress Transport) model was used as the turbulence model. The working fluid was water. The computational model is shown in Fig. 5, and the total computational region is shown in Fig. 6. The latter includes the composite body (the runner and collection device), the middle region, and the external region. To assess the potential performance of the calculation object, we assumed that a uniform flow entered the extensive space (external region) in which the calculation object was placed. Obviously, the effect of free surface and velocity distribution in the open channel is not considered. The external region is cylindrical with a diameter 10 times the outer diameter of the runner. Moreover, the lengths upstream and downstream are 10 times and 15 times the length of the outer diameter of the runner, respectively, and are measured from the center of the runner. The total computational grid consisted of about 3.67×10^6 elements for runner A and about 3.33×10^6 elements for runner B. Both steady- and unsteady-analyses used the same number of elements. To investigate grid dependence, the number of computational grids of the composite body was increased by 1.5 times, and analysis was conducted at $\lambda = 6.5$.

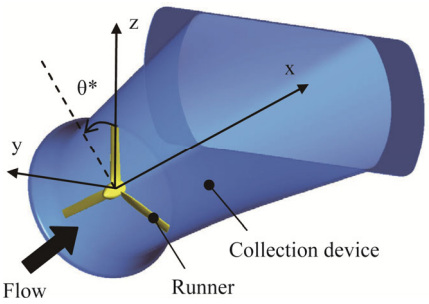

Fig. 5 Computational model

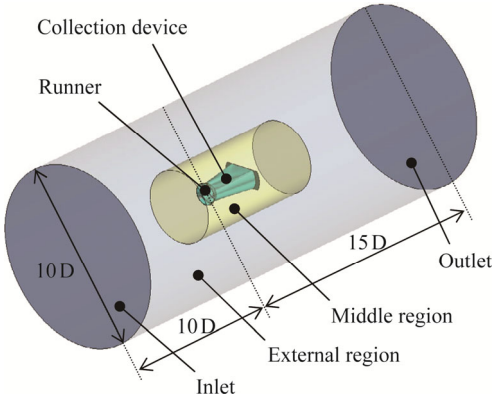

Fig. 6 Computational domain

Although the torque increased by only 5.1% from the result presented in this paper, the effect of computational grid number was comparatively small[10]. The boundary conditions were velocity v_∞ of 1.5 m/s at infinite distance for the inlet boundary condition, the rotational speed for the runner, and a static pressure of 0 Pa for the outlet boundary. For wall surface boundaries, the outer periphery of the external region was assigned as the slip condition and the other wall surfaces as nonslip. The boundaries between the rotating and static systems were joined using the frozen rotor technique in steady analyses, and the transient rotor–stator[20] technique in unsteady analyses. In steady analyses, the blade phase angle θ* was fixed to 0°.

Results and Discussion

Comparison of Performance Characteristics

Correlations between the tip speed ratio λ and the power coefficient C_W for runners A and B are shown in Fig. 7 for unsteady flow analysis. Here, the pressure and the wall shear stress acting on the blade surface were multiplied by the radius, and integrated to obtain the torque. For runner A, the maximum value of C_W was 0.527 at $\lambda = 6.5$ in steady flow and 0.573 at $\lambda = 6.5$ in unsteady flow. For runner B, the maximum value of C_W was 0.531 at $\lambda = 6.5$ in steady flow and 0.645 at $\lambda = 8.5$ in unsteady flow. That is, in unsteady flow, the maximum values of C_W for runners A and B increased by about 8.8% and 21.4%, respectively, compared to the values in steady flow. The power coefficient C_W at $\lambda = 6.5$ for runner B in unsteady flow also increased by approximately 13.2% compared to the value in steady flow.

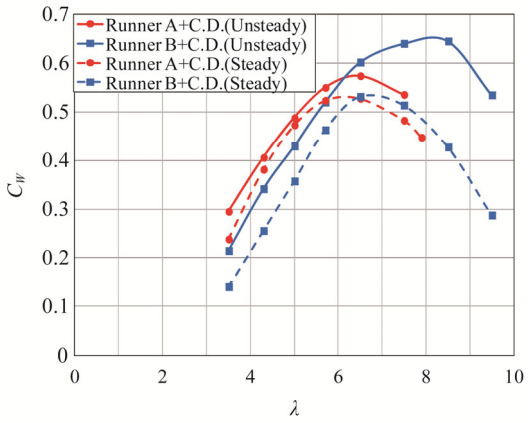

Fig. 7 Correlation between the tip speed ratio and the power coefficient

Comparing the two runners during an unsteady flow, the maximum value for runner B shifted to the high tip speed ratio side and thus improved by approximately 12.4% compared to that for runner A. For $\lambda = 6.5$, the power coefficient C_W for runner B increased by approximately 4.9% compared to that for runner A. The tip speed ratio λ for which the power coefficient C_W was a maximum for runner B during an unsteady flow differed from that during a steady flow. This suggests that runner B is more sensitive to an unsteady flow than runner A. To investigate sensitivity to an unsteady flow, we focus on the tip speed ratio $\lambda = 6.5$ that gave the maximum power for runner A.

Fluctuations in the power coefficient C_W at $\lambda = 6.5$ over one rotation of each runner are shown in Fig. 8 for both unsteady and steady flows. During an unsteady flow, runner A had very small fluctuations in C_W; the difference between the maximum and minimum values was about 0.8%. In contrast, runner B during an unsteady flow had large fluctuations in C_W; $C_W = 0.620$ at $\theta^* = 90°$ and $C_W = 0.619$ at $\theta^* = 270°$, but $C_W = 0.580$ at $\theta^* = 0°$, 180°, and 360°. Consequently, the power coefficient C_W at $\theta^* = 90°$ was approximately 6.9% larger than C_W at $\theta^* = 0°$. In next section, we discuss the power increase during an unsteady flow, the power improvement of runner B compared with that for runner A, and the fluctuations of runner B.

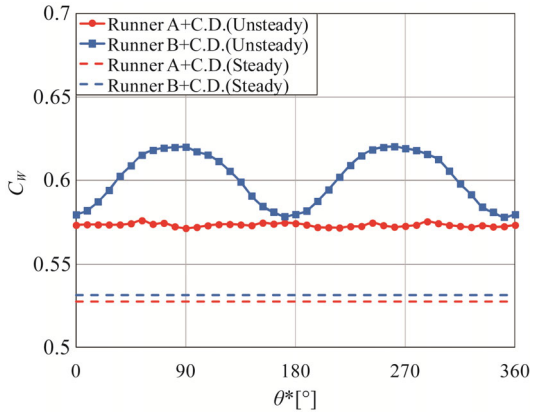

Fig. 8 Power coefficient fluctuation at $\lambda = 6.5$

Fluctuations in Various Characteristics and the Flow Field

The power coefficient C_W and the input power coefficient C_I are obtained by the following equations[8],

$$C_W = \frac{W}{\rho A v_\infty^3 / 2} = \eta C_I \tag{1}$$

$$C_I = \frac{\left(\overline{P_1} - \overline{P_2}\right) Q}{\rho A v_\infty^3 / 2} = \psi K^3 \left(1 - \nu^2\right) \tag{2}$$

where η is the turbine efficiency, ν is the hub ratio, and ψ is the loading coefficient.

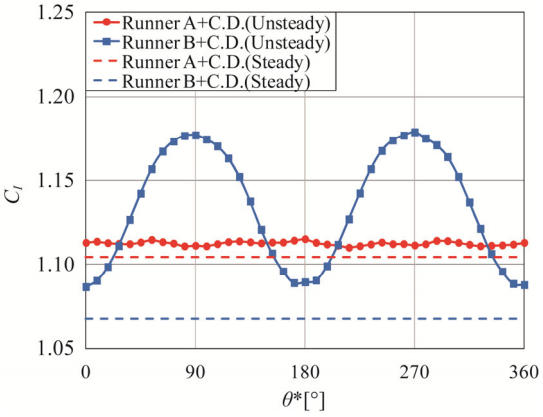

Fig. 9 Input power coefficient fluctuation at $\lambda = 6.5$

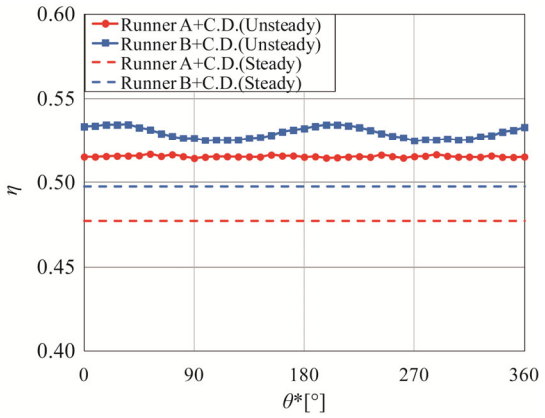

Fig. 10 Turbine efficiency fluctuation at $\lambda = 6.5$

Figures 9 and 10 show fluctuations in the input power coefficient C_I at $\lambda = 6.5$ during one rotation of each runner and fluctuations in turbine efficiency η during unsteady and steady flows, respectively. For runner A, fluctuations in C_I and η were negligible; the time average of C_I during an unsteady flow was 0.8% larger than that during a steady flow. Thus, the increase in C_W for an unsteady flow, compared to that during a steady flow, appears to be caused by an increase in η.

In contrast, for runner B, the values of the input power coefficient C_I were relatively close at the blade positions of $\theta^* = 0°$, 180°, and 360° during both unsteady and steady flows. However, the input power coefficient C_I was considerably larger at $\theta^* = 90°$ and 270° during an unsteady flow. Specifically, the input power coefficient C_I at $\theta^* = 90°$ was approximately 8.3% larger than that at $\theta^* = 0°$. During an unsteady flow, the fluctuations in η were about 1.8% at the maximum, and they had an inverted phase relative to the fluctuations in C_W and C_I. For runner B, the fluctuation in C_W apparently stems from that in C_I. Time average values for C_I and η during an unsteady flow increased by approximately 6.4% and 6.4%, respectively, compared to those during a steady flow. This increase in C_W is attributed not only to the increase in η but also to the increase in C_I; both contributed to the same extent.

Comparing both runners during an unsteady flow, the time average values for C_I and η for runner B improved by about 2.1% and 2.7%, respectively, when compared with those for runner A. Both factors contributed to the output power of runner B to the same extent.

To further consider factors that contributed to the fluctuations in C_I, fluctuations in the loading coefficient ψ and the inlet velocity ratio K are shown in Figs. 11 and 12, respectively, for one rotation of each runner at $\lambda = 6.5$ during both unsteady and steady flow. Figure 12 shows that fluctuations in K were negligible for both runners during an unsteady flow. However, time average values of K decreased by factors of 0.948 and 0.961 compared with the steady flow values, respectively; furthermore, the input power coefficients C_I decreased in proportion to the third power of these ratios. Time–average values of ψ for runners A and B during an unsteady flow were about 18.4% and 19.9% larger, respectively, than those during a steady flow. Accordingly, the increase in C_I for runner B during an unsteady flow, compared to that during a steady flow, is attributed to the relatively large increase in ψ, compared to the influence of the decrease in K.

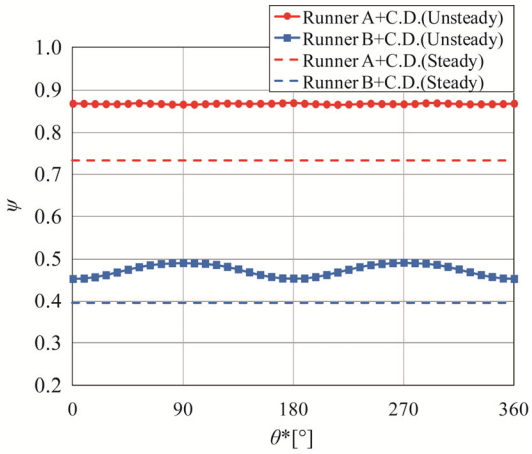

Fig. 11 Loading coefficient fluctuation at $\lambda = 6.5$

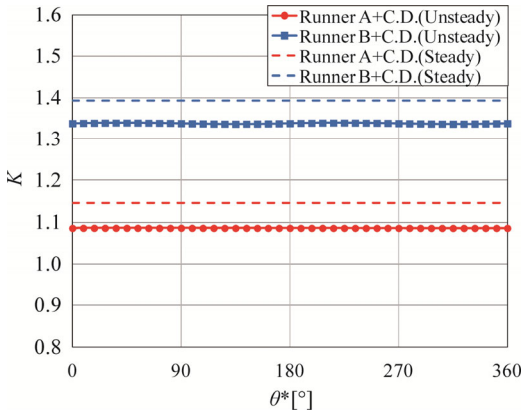

Fig. 12 Inlet velocity ratio fluctuation at $\lambda = 6.5$

The comparison of runners A and B during an unsteady flow reveals that the loading coefficient ψ for runner B was smaller than that for runner A; this was due to the smaller number of blades on runner B. Inversely, the inlet velocity ratio K for runner B was larger because it encountered less resistance than runner A. Therefore, this large inlet velocity of runner B contributes to the improvement in output power.

Fluctuations in ψ for runner A during an unsteady flow were small; thus, the difference in the maximum and minimum values was approximately 0.4%. In contrast, for runner B, the fluctuations in ψ were large, and the loading coefficient ψ at $\theta^* = 90°$ was approximately

8.3% larger than that at $\theta^* = 0°$. Therefore, fluctuations in the input power coefficient C_I for runner B during an unsteady flow were caused by fluctuations in the loading coefficient ψ.

For runner B during an unsteady flow, static pressure distributions of an x–z cross section at $\theta^* = 0°$ and an x–y cross section at $\theta^* = 90°$ at $\lambda = 6.5$ are shown in Figs. 13(a) and 13(b), respectively. The x–z cross section at $\lambda = 6.5$ for runner B during a steady flow is illustrated in Fig. 14. Focusing on the results for unsteady flow, a low-pressure region in the x–y cross section at $\theta^* = 90°$ immediately behind the blades increased relative to that of the x–z cross section at $\theta^* = 0°$. This apparently means that the low-pressure region immediately behind the blades expanded due to a diffuser effect because the tips of the blades were located in the diffuser section of the collection device at $\theta^* = 90°$. This expansion of the low-pressure region contributed to the increase in ψ, thereby being a factor that caused fluctuations in ψ to depend on the position of the blades. Moreover, comparing the unsteady and steady flow results for the x–z cross section at $\theta^* = 0°$, the low-pressure region immediately behind the blades was considerably reduced in steady flow. This suggests a reduction in interference between the runner and the collection device. For this reason, the loading coefficient ψ during a steady flow became extremely small, caused the increase in ψ during an unsteady flow, and eventually influenced the increase in the input power coefficient C_I.

Conclusions

We have investigated performance characteristics and flow fields of an axial flow hydraulic turbine with appended collection devices. The effects of two types of blades were studied during both unsteady and steady flows. Our results can be summarized as follows.

(1) The maximum output power coefficients for three-blade and two-blade runners during unsteady flow increased by about 8.8% and 21.4%, respectively, compared with those during steady flow. For the three-blade runner, the increase in output power coefficient was attributed to an increase in turbine efficiency. For the two-blade runner, increases in both turbine efficiency and input power coefficient contributed to the increase in the output power coefficient.

(2) For the two-blade runner, the loading coefficient was smaller than that for three blades, but the inlet velocity ratio for the two-blade runner was larger. This larger inlet velocity improved not only the input power coefficient but also turbine efficiency, so the power coefficient for the two-blade runner improved compared with that for the three-blade runner.

(3) Fluctuations in the power coefficient for the three-blade runner were very small. The power coefficient for the two-blade runner showed large fluctuations, with small values at blade phase angles $\theta^* = 0°$, 180°, and 360°, and large values at $\theta^* = 90°$ and 270°.

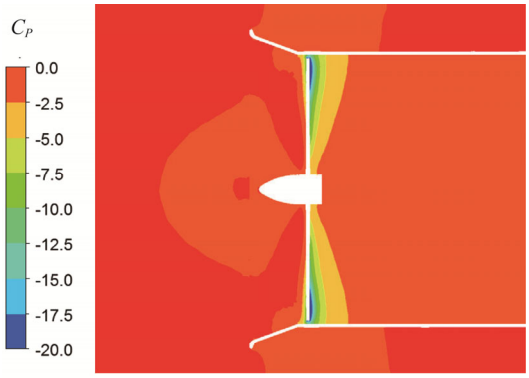

(a) x–z section, $\theta^* = 0$

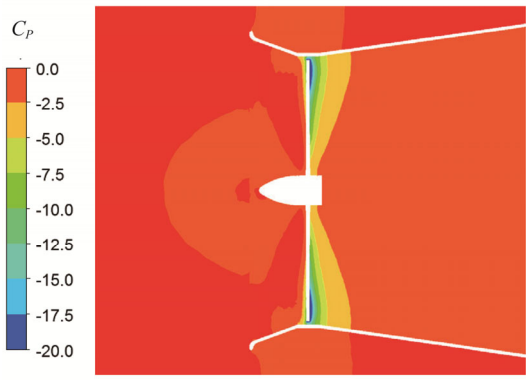

(b) x–y section, $\theta^* = 90$

Fig. 13 Static pressure distributions of Runner B at $\lambda = 6.5$ (Unsteady)

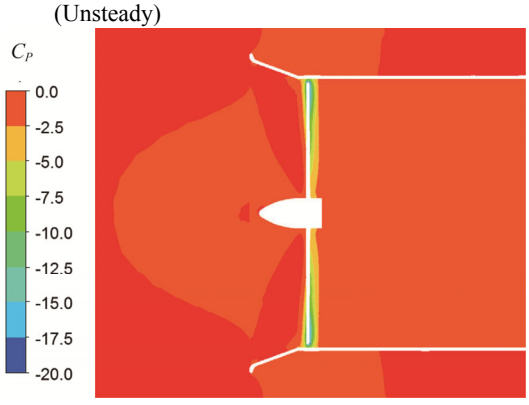

Fig. 14 Static pressure distribution of Runner B at $\lambda = 6.5$ (Steady, x-z section, $\theta^* = 0$)

(4) Fluctuations in the power coefficient for the two-blade runner were caused by fluctuations in the loading coefficient. These fluctuations in the loading coefficient stem from interference between the runner and the collection device, which had a diffuser section that was not axisymmetric.

Acknowledgment

We acknowledge that a part of the study has been subsidized by Program for Revitalization Promotion, JST (Potential Test Type α). We express our gratitude here.

References

[1] Nicolet C., Zobeiri A., Maruzewski P. and Avellan F., Experimental Investigations on Upper Part Load Vortex Rope Pressure Fluctuations in Francis Turbine Draft Tube, *International Journal of Fluid Machinery and Systems*, Vol. 4, No. 1, 2011, pp. 179–190.

[2] Reynolds T. S., Stronger Than A Hundred Men: A History of the Vertical Water Wheel, *The Johns Hopkins University Press*, Baltimore, Maryland, 1983.

[3] Fujiwara Y., Kado H. and Hosokawa Y., History and Performance of Traditional Water wheel in Western Europe, *Transactions of the Japan Society of Mechanical Engineers*, Vol. 90, No. 819, 1987, pp. 212–218.

[4] Capecchi D., Over and Undershot Waterwheels in the 18th Century. Science-Technology Controversy, *Advances in Historical Studies*, Vol. 2, No. 3, 2013, pp. 131–139.

[5] Anyi M. and Kirke B., Evaluation of small axial flow hydrokinetic turbines for remote communities, *Energy for Sustainable Development*, Vol. 14, 2010, pp. 110–116.

[6] Inagaki A. and Kanemoto T., Performance of Gyro-Type Hydraulic Turbine Suitable for Shallow Stream, *Turbomachinery*, Vol. 33, No. 10, 2005, pp. 614–621.

[7] Nakajima M., Iio S. and Ikeda T., Performance of Savonius Rotor for Environmentally Friendly Hydraulic Turbine, *Journal of Fluid Science and Technology*, Vol. 3, No. 3, 2008, pp. 420–429.

[8] Inoue M., Sakurai A. and Ohya Y., A Simple Theory of Wind Turibine with Brimmed Diffuser, *Turbomachinery*, Vol. 30, No. 8, 2002, pp. 497–502.

[9] Nishi Y., Inagaki T., Okubo K. and Kikuchi N., Study on the Development of an Axial Flow Hydraulic Turbine with a Collection Device, *Turbomachinery*, Vol. 41, No. 4, 2013, pp. 233–241.

[10] Nishi Y., Inagaki T., Okubo K. and Kikuchi N., Study on an Axial Flow Hydraulic Turbine with Collection Device, *International Journal of Rotating Machinery*, Vol. 2014, Article ID 308058, 2014, pp. 1–11.

[11] Nishi Y., Inagaki T., Okubo K., Hirama S. and Kikuchi N., Effect of Number of Blades on Performance of an Axial Flow Hydraulic Turbine with a Collection Device, *Turbomachinery*, Vol. 42, No. 2, 2014, pp. 107–117.

[12] Ohya Y., Karasudani T. and Sakurai A., Development of High-Performance Wind Turbine with Brimmed Diffuser, *Journal of the Japan Society for Aeronautical and Space Sciences*, Vol. 50, No. 587, 2002, pp. 477–482.

[13] Toshimitsu K., Nishikawa K., Haruki W., Oono S., Takao M. and Ohya Y., PIV Measurements of Flows around the Wind Turbines with a Flanged-Diffuser Shroud, *Journal of Thermal Science*, Vol. 17, No. 4, 2008, pp. 375–380.

[14] Ohya Y. and Karasudani T., A Shrouded Wind Turbine Generating High Output Power with Wind-lens Technology, *Energies*, Vol. 3, 2010, pp. 634–649.

[15] Khan M. J., Bhuyan G., Iqbal M. T. and Quaicoe J. E., Hydrokinetic energy conversion systems and assessment of horizontal and vertical axis turbines for river and tidal applications: A technology status review, *Applied Energy*, Vol. 86, 2009, pp. 1823–1835.

[16] Gaden D. L. F. and Bibeau E. L., A numerical investigation into the effect of diffusers on the performance of hydro kinetic turbines using a validated momentum source turbine model, *Renewable Energy*, Vol. 35, 2010, pp. 1152–1158.

[17] Cui B., Song Z., Zhang Y., Jin Y. and Lin Y., Influence of Additional Device on Performance of the Marine Current Turbine, *Open Journal of Fluid Dynamics*, Vol. 2, 2012, pp. 305–310.

[18] Sun H. and Kyozuka Y., Experimental Validation and Numerical Simulation Evaluation of a Shrouded Tidal Current Turbine, *Journal of the Japan Society of Naval Architects and Ocean Engineers*, Vol. 16, 2012, pp. 25–32.

[19] Matsumiya H., Kogaki T., Iida M. and Kieda K., Development of a high performance airfoil, *Turbomachinery*, Vol. 29, No. 9, 2001, pp. 519–524.

[20] ANSYS, Inc., ANSYS CFX-Solver Modeling guide, 2010, pp. 142–145.